

## P-doped all-small-molecule organic solar cells with power conversion efficiency of 17.73%

Wanying Feng<sup>1†</sup>, Kangqiao Ma<sup>1†</sup>, Guangkun Song<sup>1</sup>, Tianyin Shao<sup>2</sup>, Huazhe Liang<sup>1</sup>, Shudi Lu<sup>1</sup>, Yu Chen<sup>3</sup>, Guankui Long<sup>2,4</sup>, Chenxi Li<sup>1</sup>, Xiangjian Wan<sup>1</sup>, Zhaoyang Yao<sup>1</sup>, Bin Kan<sup>2\*</sup> & Yongsheng Chen<sup>1\*</sup>

<sup>1</sup>State Key Laboratory and Institute of Element-Organic Chemistry, The Centre of Nanoscale Science and Technology and Key Laboratory of Functional Polymer Materials, Renewable Energy Conversion and Storage Center (RECAST), College of Chemistry, Nankai University, Tianjin 300071, China;

<sup>2</sup>School of Materials Science and Engineering, National Institute for Advanced Materials, Nankai University, Tianjin 300350, China;

<sup>3</sup>Beijing Synchrotron Radiation Facility, Institute of High Energy Physics, Chinese Academy of Sciences, Beijing 100043, China;

<sup>4</sup>State Key Laboratory of Luminescent Materials and Devices, South China University of Technology, Guangzhou 510640, China

Received March 29, 2023; accepted May 2, 2023; published online June 26, 2023

All-small organic solar cells (ASM OSCs) inherit the advantages of the distinct merits of small molecules, such as well-defined structures and less batch-to-batch variation. In comparison with the rapid development of polymer-based OSCs, more efforts are needed to devote to improving the performance of ASM OSCs to close the performance gap between ASM and polymer-based OSCs. Herein, a well-known p-dopant named fluoro-7,7,8,8-tetracyano-p-quinodimethane (FTCNQ) was introduced to a high-efficiency system of HD-1:BTP-eC9, and a high power conversion efficiency (PCE) of 17.15% was achieved due to the improved electrical properties as well as better morphology of the active layer, supported by the observed higher fill factor (FF) of 79.45% and suppressed non-radiative recombination loss. Furthermore, combining with the further morphology optimization from solvent additive of 1-iodonaphthalene (IN) in the blend film, the HD-1:BTP-eC9-based device with the synergistic effects of both FTCNQ and IN demonstrates a remarkable PCE of 17.73% (certified as 17.49%), representing the best result of binary ASM OSCs to date.

**organic solar cells, all-small-molecule, power conversion efficiency, p-dopant**

**Citation:** Feng W, Ma K, Song G, Shao T, Liang H, Lu S, Chen Y, Long G, Li C, Wan X, Yao Z, Kan B, Chen Y. P-doped all-small-molecule organic solar cells with power conversion efficiency of 17.73%. *Sci China Chem*, 2023, 66: 2371–2379, <https://doi.org/10.1007/s11426-023-1616-2>

### 1 Introduction

Solution-processed organic solar cells (OSCs), with multiple features such as light weight, flexibility, and semitransparency, show great promise for applications in flexible portable devices [1–4]. Thanks to the innovations of novel materials and device engineering, power conversion efficiencies (PCEs) greater than 19% have been achieved for polymer-

based OSCs, composed of polymer donors and non-fullerene small-molecule acceptors (NFAs) [5–13]. Apart from polymer-based OSCs, there is a rising trend of developing all-small-molecule (ASM) OSCs due to the distinct merits of small molecules relative to polymer counterparts, such as well-defined structures, facile purification, and pre-eminent batch-to-batch replicability [14–19]. Fortunately, ASM OSCs have advanced greatly in recent years by considerably designing small molecule donors (SMDs), such as some typical oligothiophene, benzodithiophene (BDT) and por-

<sup>†</sup>These authors contributed equally to this work.

\*Corresponding authors (email: [yschen99@nankai.edu.cn](mailto:yschen99@nankai.edu.cn); [kanbin04@nankai.edu.cn](mailto:kanbin04@nankai.edu.cn))

phyrin-based acceptor-donor-acceptor (A-D-A) SMDs [20–22]. These donors not only achieved PCEs over 10% [23,24] in fullerene-based devices but also offered 15%–17% efficiencies when matching with Y6-family acceptors (Figure S1, [Supporting Information online](#)), such as Y6 [25], BO-4Cl [26], L8-BO [27], and BTP-eC9 [21], making the ASM OSCs a very competing candidate for future commercial application. But such performance is still significantly behind that of polymer-based OSCs.

To further improve the PCE of ASM OSCs, great efforts are necessary to design better chemical structures of SMDs as well as control their corresponding active layer morphology [28,29]. Thus far, BDT-based SMDs dominate the majority of the high-performing ASM OSCs, which can be ascribed to their easily-modified chemical structures, effective conjugated backbones, and excellent charge transport abilities [15,21,27]. Recently, we reported a new series of A-D-A type SMDs with a thiazole conjugated side group on the central BDT unit [30]. By fine-tuning the alkylthio side-chains on the thiazole unit, a small-molecular donor HD-1 with 5-((2-hexyldecyl)thio)thiazole conjugated side-chains demonstrated suitable energy level and molecular stackings, contributing to a high PCE of 17.19% in ASM OSCs [30,31].

In this contribution, based on the blending film of HD-1:BTP-eC9, a well-known p-dopant named fluoro-7,7,8,8-tetracyano-*p*-quinodimethane (FTCNQ) was introduced into the active layer to tune its electrical and morphological properties. As a result, the ASM OSC based on FTCNQ-treated blend film yields a PCE of 17.15% with an obviously higher fill factor (FF) of 79.45% and suppressed non-radiative recombination loss along with an increased open-circuit voltage ( $V_{OC}$ ) of 0.843 V. Simultaneously, the application of 1-iodonaphthalene (IN) in the active layer could regulate the morphology and enables an ordered bi-continuous interpenetrating network. Impressively, the synergistic effects of FTCNQ and IN on the active layer lead to an outstanding PCE of 17.73% with a certified value 17.49% for the HD-1:BTP-eC9-based device, representing the best result for binary ASM OSCs reported so far.

## 2 Results and discussion

### 2.1 Electro-optical properties of the molecules

[Figure 1a](#) shows the chemical structures of small molecules HD-1, BTP-eC9, and FTCNQ, respectively [31]. As observed in [Figure 1b](#), the main absorption profiles of HD-1 and BTP-eC9 are found at 450–700 and 600–950 nm, respectively, which shows a broad and complementary absorption for their blend films. The energy levels of HD-1, BTP-eC9 [32], and FTCNQ calculated from their cyclic voltammetry curves (Figure S2) are diagrammed in [Figure 1c](#). The highest occupied molecular orbital (HOMO) and

lowest unoccupied molecular orbital (LUMO) energy levels of HD-1 are calculated to be  $-5.31$  and  $-3.46$  eV, respectively. The HOMO and LUMO energy offsets between HD-1 and BTP-eC9 are both over 0.30 eV, which can guarantee strong drive force for the exciton separation [33].

### 2.2 Device performance

ASM-OSCs based on HD-1:BTP-eC9 were fabricated by adopting a conventional architecture of indium tin oxide (ITO)/poly(3,4-ethylenedioxythiophene):poly(4-styrenesulfonate) (PEDOT:PSS)/active layer/PDINO/Ag, and the detailed procedures were described in the [Supporting Information online](#). After fine-tuning the donor-to-acceptor ratios and the temperatures of thermal annealing (Tables S1 and S2, [Supporting Information online](#)), the HD-1:BTP-eC9 based control device without any additive yielded a promising PCE of 16.62% with a  $V_{OC}$  of 0.834 V, short-circuit current density ( $J_{SC}$ ) of  $25.95 \text{ mA cm}^{-2}$ , and FF of 76.81%. The p-doping strategy has been proven to be an effective method to optimize the electrical properties and device performance in many optoelectronic devices [34–37]. Thus, a well-known p-dopant compound FTCNQ was introduced into the active layer, which surprisingly promoted the PCE up to 17.15% along with a high FF of 79.45% (Table S3). Meanwhile, the application of traditional solvent additive IN can also improve the device performance to over 17% with slightly enhanced  $V_{OC}$ ,  $J_{SC}$ , and FF, simultaneously. Based on these, FTCNQ and IN were employed together to boost the device performance, which leads to a record PCE of 17.73% with a higher  $J_{SC}$  of  $26.20 \text{ mA cm}^{-2}$  and an outstanding FF greater than 80%, ultimately (Table S4). In addition, compared with the HD-1:BTP-eC9 based control device without any additive, the device with FTCNQ & IN exhibits a relatively lower series resistance ( $R_S$ ) and a higher shunt resistance ( $R_{SH}$ ), indicating a better ohmic contact and thus leading to a higher FF and PCE (Table S5) [38]. Furthermore, such a device offered a certified PCE of 17.49% subject to the calibration procedures of the National Photovoltaic Industry Metrology and Testing Center (NPVM) of China (see the certified report in the [Supporting Information online](#)), which represents the highest PCE of the current binary ASM-OSCs ([Figure 1d](#) and Table S6). The corresponding current density-voltage ( $J-V$ ) plots are displayed in [Figure 1e](#) and the detailed device parameters are presented in [Table 1](#). Besides, as shown in [Figure 1f](#) and [Figure S3](#), the distributions of PCE,  $V_{OC}$ ,  $J_{SC}$ , and FF for different conditions confirm the reliability of the excellent device performance. Meanwhile, the HD-1:BTP-eC9/FTCNQ&IN devices exhibited better storage stability in the glove box at 25 °C than that of HD-1:BTP-eC9 without any additive ([Figure S4](#)). More importantly, the ASM-OSC based on HD-1:BTP-eC9 show much less dependence with active layer

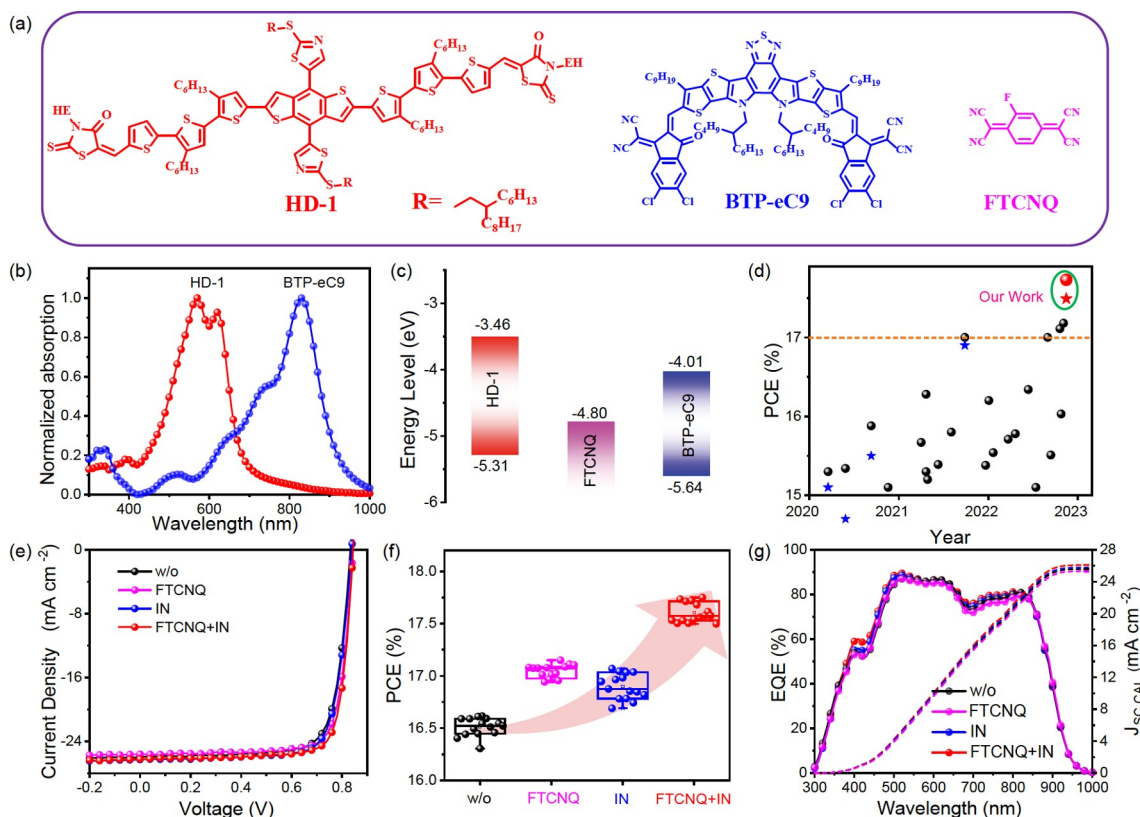


**Figure 1** (a) Chemical structures of HD-1, BTP-eC9, and FTCNQ, respectively; (b) normalized absorption spectra of HD-1 and BTP-eC9 thin films; (c) energy level diagrams of HD-1, BTP-eC9, and FTCNQ; (d) the state of the art ASM-OSCs with PCEs over 15% in literatures (the ball symbols represent literature PCEs and the red star symbol represents the corresponding certified PCE in this work); (e)  $J$ - $V$  curves; (f) PCE distributions and (g) EQE curves of the devices with/without different additives (w/o, FTCNQ, IN, and FTCNQ & IN, respectively) (color online).

**Table 1** Photovoltaic parameters and charge mobilities of optimized HD-1:BTP-eC9-based devices with/without different additives

Additive	$V_{OC}$ (V)	FF (%)	$J_{SC}$ ( $\text{mA cm}^{-2}$ )	$J_{SC, CAL}^a$ ( $\text{mA cm}^{-2}$ )	PCE <sup>b</sup> (%)	$\mu_n/\mu_c$ ( $10^{-4} \text{ cm}^2 \text{ V}^{-1} \text{ s}^{-1}$ )
w/o	0.834	76.81	25.95	25.58	16.62 (16.51±0.09)	3.92/6.73
FTCNQ	0.843	79.45	25.60	25.30	17.15 (17.04±0.06)	8.73/9.95
IN	0.838	77.50	26.28	25.78	17.07 (16.90±0.12)	5.33/7.74
FTCNQ&IN	0.844	80.19	26.20	26.09	17.73 (17.60±0.09)	9.87/11.1
FTCNQ&IN <sup>c</sup>	0.840	79.18	26.29	—	17.49	—

a) Current density calculated from EQE curves; b) average values with standard deviations obtained from 15 devices; c) certified by NPVM, Fujian, China (see the certified report in the [Supporting Information online](#)).

thickness and still exhibits a satisfactory PCE of 15.70% up to 320 nm (Figure S5 and Table S7).

The external quantum efficiency (EQE) spectra of the devices were recorded to verify their different  $J_{SC}$ , and the calculated integrated  $J_{SC,CAL}$  values agree well with the current densities from  $J$ - $V$  curves within 2% deviation range. As shown in [Figure 1g](#), all devices displayed similar and broad photon-electrical response ranges extended to  $\sim 950$  nm, which can be mainly ascribed to the contribution of BTP-eC9. Though an efficient photo-electron conversion process

already occurred in the device without any additive as supported by its high EQE values of over 80%, the enhanced absorbance strength of the blend films processed with IN or FTCNQ&IN contributed to the higher EQE values and thus higher  $J_{SC,CAL}$  values of the corresponding devices (Figure S6).

### 2.3 Evidence for p-doping in active layer

Apparently, the FTCNQ-processed devices demonstrate

improved photovoltaic performances with the simultaneously improved  $V_{OC}$  and  $FF$  while still maintaining almost the same value for  $J_{SC}$ . Note that FTCNQ with a low-lying LUMO energy level ( $-4.80$  eV) is well-known as an electron acceptor with a strong electron affinity, and its derivatives have been successfully applied as p-dopants to enhance the performance of many optoelectronic devices [39,40]. To confirm that, the ultraviolet photoelectron spectroscopy (UPS) experiment (Figure S7a, b) was conducted and the results were shown in Figure 2a and Figure S7c. Compared with HD-1 pure film, the film with FTCNQ shows a clearly increased work function (WF) of  $4.64$  eV, indicating the corresponding Fermi level ( $E_F$ ) down shifted. However, almost no WF difference is found in the BTP-eC9 films without and with FTCNQ (Figure S7c). Besides, the successfully doping of HD-1 by FTCNQ was also verified by measuring the electrical conductivity of thin films [41,42]. The measured average electrical conductivities are  $5.68 \times 10^{-6}$  and  $8.94 \times 10^{-6}$  S  $cm^{-1}$  for HD-1 films without and with FTCNQ, respectively, while the electrical conductivity values almost unchanged for BTP-eC9 films with and without FTCNQ (Figure S7d). Therefore, it can be concluded that FTCNQ serves as an effective p-dopant for the HD-1 component in the HD-1:BTP-eC9 blend films [43,44].

## 2.4 Energy loss analysis

Note the absorption pattern and range are almost completely the same with FTCNQ and IN in the solid films (Figure S6). Thus, to understand the difference in  $V_{OC}$  values of all these devices, particularly the clear increased  $V_{OC}$  with FTCNQ doping, their energy losses ( $E_{loss}$ s) were investigated in detail. The total  $E_{loss}$  can be divided into three parts according to the detailed balance theory [45]:

$$\begin{aligned} E_{loss} &= E_g - qV_{OC} \\ &= (E_g - qV_{OC}^{SQ}) + (qV_{OC}^{SQ} - qV_{OC}^{rad}) + (qV_{OC}^{rad} - qV_{OC}) \\ &= \Delta E_1 + \Delta E_2 + \Delta E_3 \end{aligned} \quad (1)$$

where  $E_g$  of these devices were determined at the intersection of absorption and photoluminescence (PL) [46], and  $q$  is the element charge. The first-term ( $\Delta E_1 = E_g - qV_{OC}^{SQ}$ ) represents the unavoidable radiative loss originating from absorption above the  $E_g$ . Here the  $V_{OC}^{SQ}$  is the theoretical maximum voltage based on the Shockley-Queisser (SQ) limit [47]. The second-term ( $\Delta E_2 = qV_{OC}^{SQ} - qV_{OC}^{rad}$ ) can be regarded as radiative recombination loss caused by sub-gap states absorption below the  $E_g$ .  $V_{OC}^{rad}$  is the open circuit voltage when there is only radiative recombination, which could be calculated from the highly sensitive EQE spectrum using the detailed balance theory. The final part of energy loss ( $\Delta E_3 = qV_{OC}^{rad} - qV_{OC}$ ) comes from the non-radiative re-

combination, which also can be calculated from the EL quantum efficiency ( $EQE_{EL}$ ) via:

$$\Delta E_3 = -kT \ln(EQE_{EL}) \quad (2)$$

The further detailed calculations are provided in the [Supporting Information online](#).

The detailed energy losses are summarized in Figure 2c and Table S8. Note, based on the absorption and PL spectra as shown in Figure S8 and Table S8, the  $E_g$  of all blend films with/without different additives are measured the same as  $1.385$  eV. As a result, the  $E_{loss}$  of devices under such four different conditions are calculated to be  $0.551$ ,  $0.542$ ,  $0.547$ , and  $0.540$  eV, respectively. Here, the  $\Delta E_1$ , which is only determined by the  $E_g$ , is equal to  $0.261$  eV for all devices. Meanwhile, the incorporation of FTCNQ and IN did not cause any additional absorption of sub-gap states in FTPE-EQE measurement (Figure S9a), which indicates the radiative recombination loss ( $\Delta E_2$ ) of optimized devices with doping/additive very close to the control device ( $\sim 0.07$  eV) [48,49]. Thus, the non-radiative recombination loss  $\Delta E_3$  is the main reason for their difference in the  $V_{OC}$  of all the devices (Figure 2c). As displayed in Figure S9b, the FTCNQ-treated device exhibited a significantly increased  $EQE_{EL}$  compared with the control device, indicating a reduced  $\Delta E_3$  of  $0.213$  eV (Table S8). Note that molecular doping is widely accepted as an effective way to reduce the trap density [50], and low trap density within bulk-heterojunction (BHJ) OSCs could reduce the non-radiative recombination ratio and then decrease the energy loss of OSCs [51–53]. Therefore, the reduced  $\Delta E_3$  of the FTCNQ-treated device should be originated from the p-doping of FTCNQ. Meanwhile, the introduction of IN also slightly reduced the  $\Delta E_3$  to  $0.221$  eV, which might be caused by the improved morphology as discussed below. Consequently, the device treated with both FTCNQ and IN achieved the smallest  $\Delta E_3$  of  $0.211$  eV by the synergistic improvements of electrical properties and morphology, leading to its enhanced  $V_{OC}$ .

## 2.5 Charge dynamics

The function of the photocurrent density ( $J_{ph}$ ) versus the effective voltage ( $V_{eff}$ ) was measured to investigate the behaviors of exciton dissociation and charge extraction in the OSCs according to the reported method (Figure S10a) [54]. The device treated with FTCNQ showed a slightly lower exciton dissociation efficiencies ( $P_{diss}$ ) value compared with the other three devices, which may be the reason for its slightly reduced  $J_{SC}$ . But the devices treated with FTCNQ, IN or both FTCNQ and IN exhibited higher charge extraction efficiencies ( $P_{coll}$ ) than the control device, which implied a more efficient charge extraction process, supporting their higher FFs. The light-intensity ( $P_{light}$ )-dependent  $J_{SC}$  and  $V_{OC}$  measurements were further carried out to identify the charge

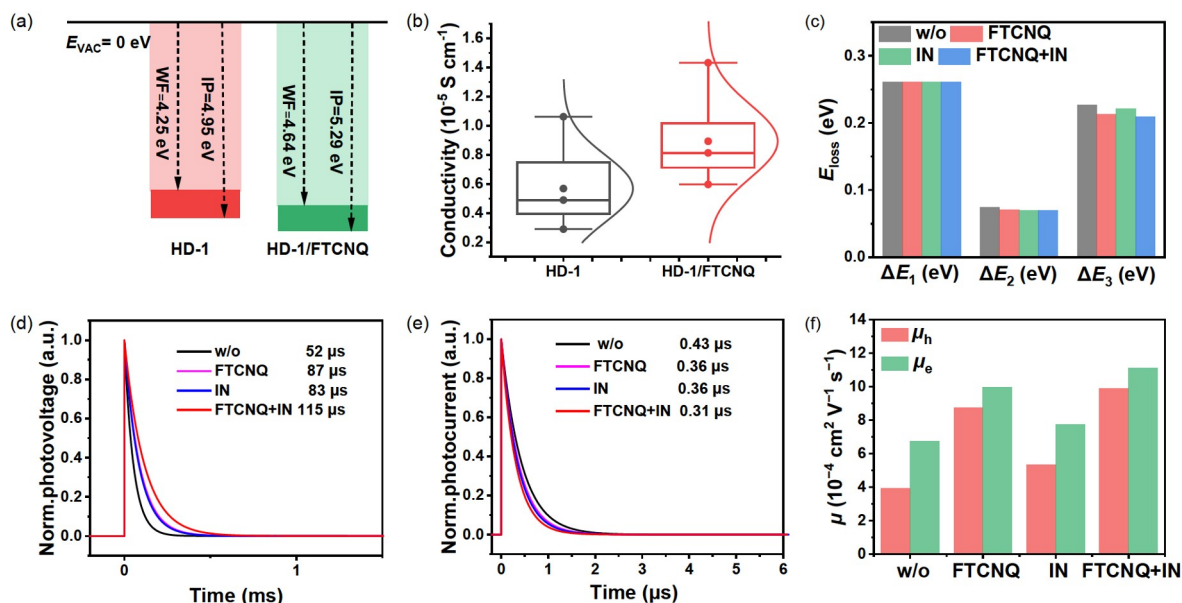


**Figure 2** (a) WF and  $E_f$  results from UPS measurement and (b) electrical conductivity distribution (20 devices) of HD-1 films with/without 2.0 wt% FTCNQ; (c) energy loss, (d) transient photovoltage, (e) transient photocurrent measurements, and (f) charge mobility of HD-1:BTP-eC9 blend films under different conditions (w/o, FTCNQ, IN, and FTCNQ&IN, respectively) (color online).

recombination mechanism. It has been demonstrated that the bimolecular recombination and trap-assisted recombination can be evaluated using the power-law relations of  $J_{SC}$  vs.  $P_{light}^\alpha$  and  $V_{OC}$  vs.  $nkT/q\ln(P_{light})$ , respectively [54,55]. As result, the corresponding  $\alpha$  factors of all devices were measured and were close to unit (Figure S10b), revealing their similar and negligible bimolecular recombination. In comparison to the control device with the  $n$  of 1.22 derived from the relationship between  $V_{OC}$  and  $P_{light}$  (Figure S10c), all the other devices showed lower  $n$  values, which were 1.18, 1.20, and 1.16 for devices with FTCNQ, IN, and FTCNQ&IN, respectively, suggesting their suppressed trap-assisted recombination.

Transient photovoltage (TPV) and transient photocurrent (TPC) measurements were conducted to evaluate the impact of doping/additive treatments on the charge carrier lifetime and charge extraction time of the devices (Figure 2d, e) [56]. In comparison with the control device, the introduction of FTCNQ and IN both prolonged the charge carrier lifetime and shortened the charge extraction time. The devices processed with FTCNQ&IN together showed the longest charge carrier lifetime of 115  $\mu$ s and the shortest charge extraction time 0.31  $\mu$ s. Apparently, the synergistic effect of FTCNQ and IN is much more beneficial for improving the charge transport and charger extraction, favoring its higher  $J_{SC}$  and FF, simultaneously.

Besides, the hole ( $\mu_h$ ) and electron ( $\mu_e$ ) mobilities of HD-1:BTP-eC9 films upon doping with FTCNQ, which can be estimated by the space charge limited current (SCLC) method (Figure S11), became clearly higher than those of undoped pristine blend films (Figure 2f and Table 1). As

shown in Table 1, doping from FTCNQ clearly increased the  $\mu_h$  by 123%, from  $3.92 \times 10^{-4} \text{ cm}^2 \text{ V}^{-1} \text{ s}^{-1}$  in a pristine film to  $8.73 \times 10^{-4} \text{ cm}^2 \text{ V}^{-1} \text{ s}^{-1}$  in the FTCNQ-doped film, while an increase of  $\mu_e$  by 48%, from  $6.73 \times 10^{-4} \text{ cm}^2 \text{ V}^{-1} \text{ s}^{-1}$  in a pristine film to  $9.95 \times 10^{-4} \text{ cm}^2 \text{ V}^{-1} \text{ s}^{-1}$  in the FTCNQ-doped film. These observed improved charge mobilities should be mainly caused by the p-doping of FTCNQ [57]. Also, the  $\mu_h$  and  $\mu_e$  of the blend film treated with IN were slightly improved to  $5.33 \times 10^{-4}$  and  $7.74 \times 10^{-4} \text{ cm}^2 \text{ V}^{-1} \text{ s}^{-1}$ , respectively, compared with those of pristine blend films due to the improved morphology as discussed below. When combined with the doping of FTCNQ and morphology tuning of IN together, the  $\mu_h$  and  $\mu_e$  are further enhanced to  $9.87 \times 10^{-4}$  and  $1.11 \times 10^{-3} \text{ cm}^2 \text{ V}^{-1} \text{ s}^{-1}$ , respectively. Besides, as compared to the blend films without doping/additive, more balanced charge mobilities were observed for the blend films upon FTCNQ-doping, which can well explain their significantly improved FFs [58].

Femtosecond transient absorption (TA) spectroscopy was employed to investigate the charge transfer dynamics [59–62] in the HD-1:BTP-eC9 blend films, and the corresponding TA spectra are shown in Figure 3a–d and Figure S12. The excitation wavelength at 824 nm was selected to only excite the BTP-eC9, and the TA spectra of HD-1:BTP-eC9 blend films without any additives (w/o) and treated with FTCNQ & IN are shown in Figure 3a, b. The clear bleach peaks at 846 and 921 nm appeared in HD-1:BTP-eC9 film, corresponding to the ground state bleach (GSB) and stimulated emission (SE) of BTP-eC9 after photoexcitation. With the decay of BTP-eC9 bleach peaks at 800–900 nm, a few clear GSB peaks of HD-1 at 582 and 637 nm appeared in the transient

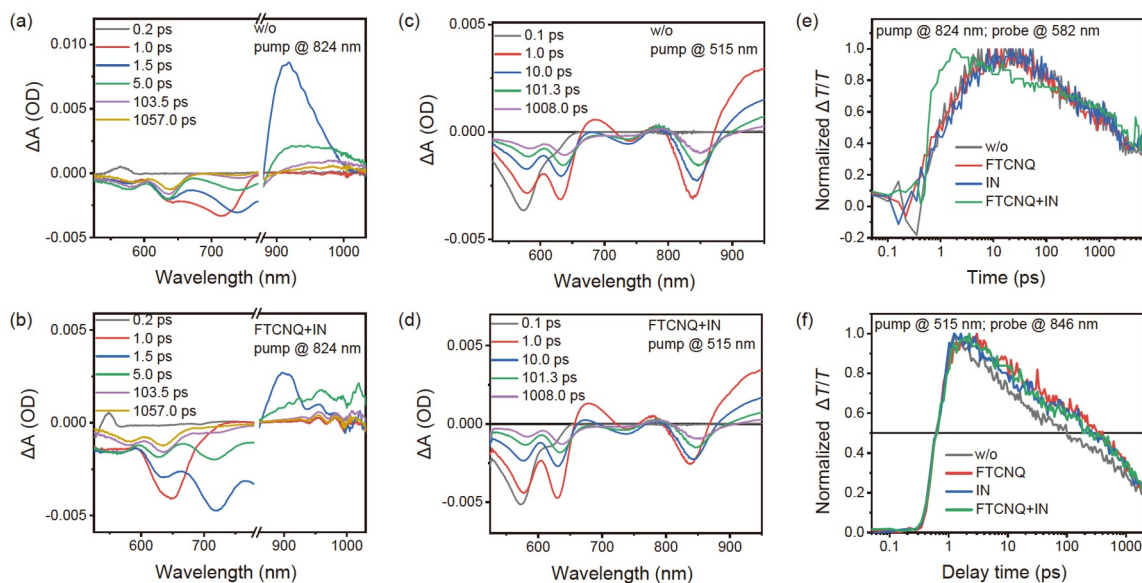


**Figure 3** Femtosecond transient absorption spectra of HD-1:BTP-eC9 blend films (a, c) treated without any additives (w/o) and (b, d) treated with FTCNQ&IN; (e) hole, and (f) electron transfer dynamics of HD-1:BTP-eC9 blend films with different treatments (color online).

absorption spectrum, confirming the observation of hole transfer from BTP-eC9 to HD-1. The hole transfer kinetics of the four blends were extracted in Figure 3e. After fitting the hole transfer kinetics, the hole transfer times of HD-1:BTP-eC9 blend films treated without any additive, with FTCNQ, IN, and FTCNQ&IN are 0.93, 1.11, 1.26, and 0.58 ps, respectively. Thus, the hole transfer of the blend films of HD-1:BTP-eC9 treated with FTCNQ&IN is the fastest, which agreed well with enhanced FF and  $J_{SC}$ , thus the PCE. However, the electron transfer dynamics are almost the same for all the HD-1:BTP-eC9 blend films (w/o, FTCNQ, IN, and FTCNQ&IN) (Figure 3c, d). As shown in Figure 3f, the electron transfer times of the blend films of HD-1:BTP-eC9 treated without any additive, with FTCNQ, IN, and FTCNQ&IN are 0.65, 0.61, 0.61, and 0.63 ps, respectively. Therefore, the blend films with different treatments mainly influence the hole transfer dynamics while exhibiting negligible impacts on the electron transfer dynamics.

## 2.6 Morphology investigation

The surface and phase separation morphologies of HD-1:BTP-eC9 blend films were characterized by atomic force microscopy (AFM) and transmission electron microscopy (TEM), respectively. As demonstrated in Figure 4a–d, all blend films were smooth with a small root-mean-square (RMS) roughness of  $\sim 0.6$  nm. While the addition of FTCNQ effectively tuned the oversize aggregation of the HD-1:BTP-eC9 blends. These features were observed in the transmission electron microscope (TEM) images as well (Figure S13a–d). Compared with the control blend film, the film with FTCNQ displayed smaller agglomerates. Meanwhile, a more

continuous interpenetrating network morphology can be achieved in the IN-treated blend film. Afterwards, a well-developed nanoscale bi-continuous interpenetrating network with fibrous structure was realized in the blend film with both FTCNQ and IN. These results indicated that both FTCNQ and IN play a beneficial role in regulating the morphologies, thus in favor of the charge dynamics and better device performance.

To investigate the effect of FTCNQ and IN on the molecular orientation and crystallinity, the two-dimensional grazing incidence wide-angle X-ray scattering (2D GI-WAXS) measurement was performed. Figure S14 shows the 2D patterns and corresponding out-of-plane (OOP) and in-plane (IP) one-dimensional (1D) profiles for the HD-1 films with and without FTCNQ. The detailed parameters of corresponding 2D GIWAXS are summarized in Table S9. The 2D patterns for the pure HD-1 film shows (010) diffraction peaks in both in-plane (IP) and out-of-plane (OOP) directions, suggesting the coexistence of face-on and edge-on orientations. The  $\pi$ - $\pi$  stacking distances calculated from the peak locations in extracted 1D profiles is estimated as 3.57 Å. The addition of FTCNQ into the HD-1 film has little impact on the molecular packing orientations but enables a tighter  $\pi$ - $\pi$  stacking with a slightly smaller distance of 3.55 Å. In addition, the crystal coherence lengths (CCL) estimated by the Scherrer equation of HD-1 film with FTCNQ doping becomes slightly larger than the pure HD-1 film in both IP and OOP directions. However, the BTP-eC9 film with FTCNQ doping shows largely unchanged  $\pi$ - $\pi$  stacking distance and even smaller CCL in both IP and OOP directions compared with BTP-eC9 pure film (Figure S15 and Table S10). These results reveal the fact that the FTCNQ

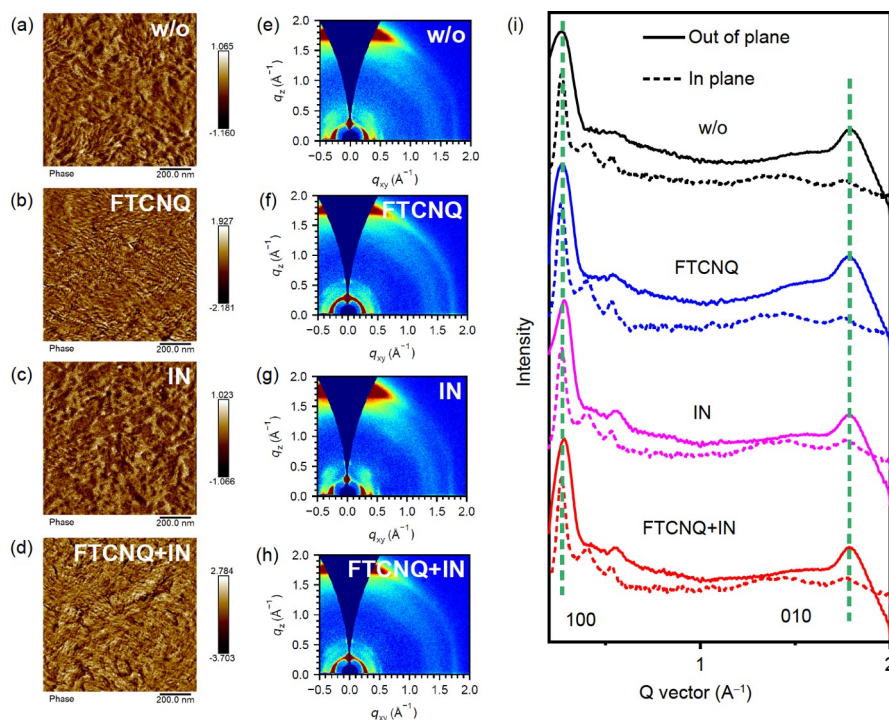


**Figure 4** (a–d) AFM phase images and (e–h) 2D GIWAXS patterns and (i) scattering profiles of the HD-1:BTP-eC9 blend films under four different treatments (w/o, FTCNQ, IN, and FTCNQ&IN, respectively) (color online).

could improve the crystallinity of HD-1.

Figure 4e–i shows the 2D GIWAXS patterns and the corresponding 1D line cutting profiles of the HD-1:BTP-eC9 blend films, and the detailed parameters are summarized in Table S11. In the blend film without any additives, a face-on dominated molecular orientation is observed as evidenced by its lamellar scattering peaks ( $h00$ ) in the IP direction and  $\pi$ - $\pi$  stacking peak (010) in the OOP direction. After introducing FTCNQ into the blend film, an annular (100) scattering pattern attributed to the lamellar packing of HD-1 is observed in the low  $q$  range of  $0.27 \text{ \AA}^{-1}$ , largely maintaining the molecular stacking orientation of the HD-1 pure film, which may result in higher phase purity and lower bulk defects [63]. As contrast, the introduction of IN hardly changes the face-on dominated molecular orientation behaviors but improve the crystallinity with a shorter lamellar stacking distance and a larger CCL in OOP direction. The improvements in molecular packing and crystallinity resulting from FTCNQ and IN can be well inherited when adopting both into the blend film. For example, the molecular stacking orientation in the HD-1 pure film is maintained to some extent in the blend films with FTCNQ&IN. Besides, the CCLs of the lamellar scattering peaks (100) in both IP and OOP direction and  $\pi$ - $\pi$  stacking (010) diffraction peak in OOP direction for the blend films with FTCNQ&IN are all increased compared to the control device, implying orderly molecular aggregation with higher crystallinity, which are beneficial for charge transport.

### 3 Conclusions

In summary, the addition of a well-known p-dopant compound FTCNQ into the high-efficiency ASM OSCs system of HD-1:BTP-eC9 not only contributed to the enhanced electronic properties (such as improved and balanced hole and electron mobilities) but also could regulate the morphological characters of the active layer. Consequently, the FTCNQ-treated device offered a maximum of PCE 17.15% with improved FF and reduced non-radiative recombination loss. Meanwhile, the solvent additive of IN optimized the morphologies, resulting in a similar PCE of over 17%. Together, the synergistic effect of FTCNQ and IN could boost the photovoltaic parameters of  $V_{OC}$ ,  $J_{SC}$ , and FF simultaneously, enabling a maximum PCE of 17.73% with a certified value of 17.49%. To our knowledge, this outstanding result is the best for binary ASM OSCs reported so far, and comparable to the BTP-eC9 based binary polymer solar cells [64–66]. These results indicate that it is highly possible, by adopting a p-doping strategy, to simultaneously improve the three determining parameters of  $V_{OC}$ ,  $J_{SC}$ , and FF for an even higher device performance of the same active material, which is a very entangled and challenging issue in the field of OSC.

**Acknowledgements** This work was supported by the Ministry of Science and Technology of the People's Republic of China (MoST, 2022YFB4200400, 2019YFA0705900) and the National Natural Science Foundation of China (21935007, 52025033, 51873089), Tianjin city (20JCZDJC00740, 22JCQNJC00530), 111 Project (B12015), the Funda-

mental Research Funds for the Central Universities, Nankai University (023-ZB22000105, 020-ZB22000110, 020-92220002), and Haihe Laboratory of Sustainable Chemical Transformations. We thank Yuanyuan Jiang and Prof. Xiaozhang Zhu for the UPS measurement.

**Conflict of interest** The authors declare no conflict of interest.

**Supporting information** The supporting information is available online at <http://chem.scichina.com> and <http://link.springer.com/journal/11426>. The supporting materials are published as submitted, without typesetting or editing. The responsibility for scientific accuracy and content remains entirely with the authors.

- Zeng G, Chen W, Chen X, Hu Y, Chen Y, Zhang B, Chen H, Sun W, Shen Y, Li Y, Yan F, Li Y. *J Am Chem Soc*, 2022, 144: 8658–8668
- Sun Y, Chang M, Meng L, Wan X, Gao H, Zhang Y, Zhao K, Sun Z, Li C, Liu S, Wang H, Liang J, Chen Y. *Nat Electron*, 2019, 2: 513–520
- Dauzon E, Sallenave X, Plesse C, Goubard F, Amassian A, Anthopoulos TD. *Adv Mater*, 2021, 33: 2101469
- Liu Y, Liu B, Ma CQ, Huang F, Feng G, Chen H, Hou J, Yan L, Wei Q, Luo Q, Bao Q, Ma W, Liu W, Li W, Wan X, Hu X, Han Y, Li Y, Zhou Y, Zou Y, Chen Y, Li Y, Chen Y, Tang Z, Hu Z, Zhang ZG, Bo Z. *Sci China Chem*, 2022, 65: 224–268
- Zhan L, Yin S, Li Y, Li S, Chen T, Sun R, Min J, Zhou G, Zhu H, Chen Y, Fang J, Ma CQ, Xia X, Lu X, Qiu H, Fu W, Chen H. *Adv Mater*, 2022, 34: 2206269
- Zhu L, Zhang M, Xu J, Li C, Yan J, Zhou G, Zhong W, Hao T, Song J, Xue X, Zhou Z, Zeng R, Zhu H, Chen CC, MacKenzie RCI, Zou Y, Nelson J, Zhang Y, Sun Y, Liu F. *Nat Mater*, 2022, 21: 656–663
- Cui Y, Xu Y, Yao H, Bi P, Hong L, Zhang J, Zu Y, Zhang T, Qin J, Ren J, Chen Z, He C, Hao X, Wei Z, Hou J. *Adv Mater*, 2021, 33: 2102420
- Fu J, Fong PWK, Liu H, Huang CS, Lu X, Lu S, Abdelsamie M, Kodalle T, Sutter-Fella CM, Yang Y, Li G. *Nat Commun*, 2023, 14: 1760
- Chen T, Li S, Li Y, Chen Z, Wu H, Lin Y, Gao Y, Wang M, Ding G, Min J, Ma Z, Zhu H, Zuo L, Chen H. *Adv Mater*, 2023, 35: 2300400
- Wang J, Wang Y, Bi P, Chen Z, Qiao J, Li J, Wang W, Zheng Z, Zhang S, Hao X, Hou J. *Adv Mater*, 2023, 35: 2301583
- Kong X, Zhang J, Meng L, Sun C, Jiang X, Zhang J, Zhu C, Sun G, Li J, Li X, Wei Z, Li Y. *CCS Chem*, 2023, 1–11
- Gao W, Qi F, Peng Z, Lin FR, Jiang K, Zhong C, Kaminsky W, Guan Z, Lee CS, Marks TJ, Ade H, Jen AKY. *Adv Mater*, 2022, 34: 2202089
- Xu X, Jing W, Meng H, Guo Y, Yu L, Li R, Peng Q. *Adv Mater*, 2023, 35: 2208997
- Kan B, Kan Y, Zuo L, Shi X, Gao K. *InfoMat*, 2020, 3: 175–200
- Tang H, Yan C, Huang J, Kan Z, Xiao Z, Sun K, Li G, Lu S. *Matter*, 2020, 3: 1403–1432
- Walker B, Tamayo AB, Dang XD, Zalar P, Seo JH, Garcia A, Tanttiwiwat M, Nguyen TQ. *Adv Funct Mater*, 2009, 19: 3063–3069
- Liu Y, Wan X, Yin B, Zhou J, Long G, Yin S, Chen Y. *J Mater Chem*, 2010, 20: 2464–2468
- Liu Y, Wan X, Wang F, Zhou J, Long G, Tian J, Chen Y. *Adv Mater*, 2011, 23: 5387–5391
- Kan B, Zhang Q, Li M, Wan X, Ni W, Long G, Wang Y, Yang X, Feng H, Chen Y. *J Am Chem Soc*, 2014, 136: 15529–15532
- Duan T, Chen Q, Yang Q, Hu D, Cai G, Lu X, Lv J, Song H, Zhong C, Liu F, Yu D, Lu S. *J Mater Chem A*, 2022, 10: 3009–3017
- Zhang L, Sun R, Zhang Z, Zhang J, Zhu Q, Ma W, Min J, Wei Z, Deng D. *Adv Mater*, 2022, 34: 2207020
- Sun Y, Nian L, Kan Y, Ren Y, Chen Z, Zhu L, Zhang M, Yin H, Xu H, Li J, Hao X, Liu F, Gao K, Li Y. *Joule*, 2022, 6: 2835–2848
- Deng D, Zhang Y, Zhang J, Wang Z, Zhu L, Fang J, Xia B, Wang Z, Lu K, Ma W, Wei Z. *Nat Commun*, 2016, 7: 13740
- Wan J, Xu X, Zhang G, Li Y, Feng K, Peng Q. *Energy Environ Sci*, 2017, 10: 1739–1745
- Guo J, Qiu B, Yang D, Zhu C, Zhou L, Su C, Jeng US, Xia X, Lu X, Meng L, Zhang Z, Li Y. *Adv Funct Mater*, 2022, 32: 2110159
- Qin J, Chen Z, Bi P, Yang Y, Zhang J, Huang Z, Wei Z, An C, Yao H, Hao X, Zhang T, Cui Y, Hong L, Liu C, Zu Y, He C, Hou J. *Energy Environ Sci*, 2021, 14: 5903–5910
- Li Z, Wang X, Zheng N, Saparbaev A, Zhang J, Xiao C, Lei S, Zheng X, Zhang M, Li Y, Xiao B, Yang R. *Energy Environ Sci*, 2022, 15: 4338–4348
- Ge J, Xie L, Peng R, Ge Z. *Adv Mater*, 2023, 34: 2206566
- Gao H, Sun Y, Meng L, Han C, Wan X, Chen Y. *Small*, 2023, 19: 2205594
- Wu S, Feng W, Meng L, Zhang Z, Si X, Chen Y, Wan X, Li C, Yao Z, Chen Y. *Nano Energy*, 2022, 103: 107801
- Ma K, Feng W, Liang H, Chen H, Wang Y, Wan X, Yao Z, Li C, Kan B, Chen Y. *Adv Funct Mater*, 2023, 33: 2214926
- Cui Y, Yao H, Zhang J, Xian K, Zhang T, Hong L, Wang Y, Xu Y, Ma K, An C, He C, Wei Z, Gao F, Hou J. *Adv Mater*, 2020, 32: 1908205
- Hou J, Inganäs O, Friend RH, Gao F. *Nat Mater*, 2018, 17: 119–128
- Yan H, Ma W. *Adv Funct Mater*, 2021, 32: 2111351
- Yurash B, Cao DX, Brus VV, Leifert D, Wang M, Dixon A, Seifrid M, Mansour AE, Lungwitz D, Liu T, Santiago PJ, Graham KR, Koch N, Bazan GC, Nguyen TQ. *Nat Mater*, 2019, 18: 1327–1334
- Xiong Y, Ye L, Gadisa A, Zhang Q, Rech JJ, You W, Ade H. *Adv Funct Mater*, 2019, 29: 1806262
- Xu X, Feng K, Yu L, Yan H, Li R, Peng Q. *ACS Energy Lett*, 2020, 5: 2434–2443
- Qi B, Wang J. *Phys Chem Chem Phys*, 2013, 15: 8972–8982
- Mun J, Kang J, Zheng Y, Luo S, Wu Y, Gong H, Lai JC, Wu HC, Xue G, Tok JBH, Bao Z. *Adv Electron Mater*, 2020, 6: 2000251
- Ma T, Dong BX, Grocke GL, Strzalka J, Patel SN. *Macromolecules*, 2020, 53: 2882–2892
- Méndez H, Heimel G, Winkler S, Frisch J, Opitz A, Sauer K, Wegner B, Oehzelt M, Röthel C, Duhm S, Töbrens D, Koch N, Salzmann I. *Nat Commun*, 2015, 6: 8560
- Cochran JE, Junk MJN, Glauddell AM, Miller PL, Cowart JS, Toney MF, Hawker CJ, Chmelka BF, Chabinye ML. *Macromolecules*, 2014, 47: 6836–6846
- Chen H, Maxwell A, Li C, Teale S, Chen B, Zhu T, Ugur E, Harrison G, Grater L, Wang J, Wang Z, Zeng L, Park SM, Chen L, Serles P, Awini RA, Subedi B, Zheng X, Xiao C, Podraza NJ, Filleter T, Liu C, Yang Y, Luther JM, De Wolf S, Kanatzidis MG, Yan Y, Sargent EH. *Nature*, 2023, 613: 676–681
- Zhang H, Zhang X, Li Y, Huang G, Du W, Shi J, Wang B, Li S, Jiang R, Zhang J, Cheng Q, Chen J, Han B, Liu X, Zhang Y, Zhou H. *Sol RRL*, 2022, 6: 2101096
- Rau U, Blank B, Müller TC, Kirchartz T. *Phys Rev Appl*, 2017, 7: 044016
- Wang Y, Qian D, Cui Y, Zhang H, Hou J, Vandewal K, Kirchartz T, Gao F. *Adv Energy Mater*, 2018, 8: 1801352
- Kirchartz T, Taretto K, Rau U. *J Phys Chem C*, 2009, 113: 17958–17966
- Liu J, Chen S, Qian D, Gautam B, Yang G, Zhao J, Bergqvist J, Zhang F, Ma W, Ade H, Inganäs O, Gundogdu K, Gao F, Yan H. *Nat Energy*, 2016, 1: 16089
- Ma X, Wang J, Gao J, Hu Z, Xu C, Zhang X, Zhang F. *Adv Energy Mater*, 2020, 10: 2001404
- Shang Z, Heumueller T, Prasanna R, Burkhard GF, Naab BD, Bao Z, McGehee CD, Salleo A. *Adv Energy Mater*, 2016, 6: 1601149
- Wöpke C, Göhler C, Saladina M, Du X, Nian L, Greve C, Zhu C, Yallum KM, Hofstetter YJ, Becker-Koch D, Li N, Heumueller T, Milekhin I, Zahn DRT, Brabec CJ, Banerji N, Vaynzof Y, Herzog EM, MacKenzie RCI, Deibel C. *Nat Commun*, 2022, 13: 3786
- Zhang Y, Cai G, Li Y, Zhang Z, Li T, Zuo X, Lu X, Lin Y. *Adv Mater*, 2021, 33: 2008134
- Chen H, Zou Y, Liang H, He T, Xu X, Zhang Y, Ma Z, Wang J, Zhang M, Li Q, Li C, Long G, Wan X, Yao Z, Chen Y. *Sci China Chem*,

- 2022, 65: 1362–1373
- 54 Kyaw AKK, Wang DH, Gupta V, Leong WL, Ke L, Bazan GC, Heeger AJ. *ACS Nano*, 2013, 7: 4569–4577
- 55 Koster LJA, Mihaiilechi VD, Ramaker R, Blom PWM. *Appl Phys Lett*, 2005, 86: 123509
- 56 Liu S, Liang Q, Yan J, Wu H, Cao Y. *Org Electron*, 2018, 59: 427–431
- 57 Raval P, Dhennin M, Vezin H, Pawlak T, Roussel P, Nguyen TQ, Manjunatha Reddy GN. *Electrochim Acta*, 2022, 424: 140602
- 58 Meresa AA, Parida B, Long DX, Kim D, Kim T, Earmme T, Hong J, Kang D-, Kim FS. *Intl J Energy Res*, 2022, 46: 8716–8725
- 59 Zhu L, Zhang M, Zhou G, Hao T, Xu J, Wang J, Qiu C, Prine N, Ali J, Feng W, Gu X, Ma Z, Tang Z, Zhu H, Ying L, Zhang Y, Liu F. *Adv Energy Mater*, 2020, 10: 1904234
- 60 Jiang K, Zhang J, Zhong C, Lin FR, Qi F, Li Q, Peng Z, Kaminsky W, Jang SH, Yu J, Deng X, Hu H, Shen D, Gao F, Ade H, Xiao M, Zhang C, Jen AKY. *Nat Energy*, 2022, 7: 1076–1086
- 61 Rao A, Chow PCY, Gélinas S, Schlenker CW, Li CZ, Yip HL, Jen AKY, Ginger DS, Friend RH. *Nature*, 2013, 500: 435–439
- 62 Chandrabose S, Chen K, Barker AJ, Sutton JJ, Prasad SKK, Zhu J, Zhou J, Gordon KC, Xie Z, Zhan X, Hodgkiss JM. *J Am Chem Soc*, 2019, 141: 6922–6929
- 63 Xu T, Lv J, Yang K, He Y, Yang Q, Chen H, Chen Q, Liao Z, Kan Z, Duan T, Sun K, Ouyang J, Lu S. *Energy Environ Sci*, 2021, 14: 5366–5376
- 64 Deng M, Xu X, Duan Y, Yu L, Li R, Peng Q. *Adv Mater*, 2023, 35: 2210760
- 65 Meng H, Jing W, Xu X, Yu L, Peng Q. *Angew Chem Int Ed*, 2023, 62: e202301958
- 66 Han C, Wang J, Zhang S, Chen L, Bi F, Wang J, Yang C, Wang P, Li Y, Bao X. *Adv Mater*, 2023, 35: 2208986